



1 **Global seismic energy scaling relationships based on the type of faulting.**

2
3

4 **Quetzalcoatl Rodríguez-Pérez¹, F. Ramón Zúñiga²**

5

6 ¹ Dirección de Desarrollo Científico, Dirección de Cátedras, Consejo Nacional de Ciencia y Tecnología, Mexico City,
7 Mexico.

8 ² Centro de Geociencias, Universidad Nacional Autónoma de México, Juriquilla, Querétaro, Mexico.

9

10 Correspondence: Quetzalcoatl Rodríguez-Pérez (quetza@geociencias.unam.mx)

11

12 **Abstract.** We derived scaling relationships for different seismic energy metrics for earthquakes with
13 $M_W > 6.0$ from 1990 to 2022. The seismic energy estimations were derived with two methodologies, the
14 first based on the velocity flux integration and the second based on finite-fault models. In the first case,
15 we analyzed 3331 reported seismic energies derived by integrating far-field waveforms. In the latter
16 methodology, we used the total moment rate functions and the approximation of the overdamped
17 dynamics to quantify seismic energy from 231 finite-fault models (E_{mrt} , and E_O , E_U , respectively). Both
18 methodologies provide compatible energy estimates. The radiated seismic energies estimated from the
19 slip models and integration of velocity records are also compared for different focal mechanisms by
20 deriving converting scaling relations among the different energy types. Additionally, the behavior of
21 radiated seismic energy (E_R), energy-to-moment ratio (E_R/M_0), and apparent stress (τ_α) for different
22 rupture types at a global scale is examined by considering depth variations of mechanical properties,
23 such as seismic velocities and rock densities, and rigidities. For this purpose, we used a 1-D global
24 velocity model. In agreement with previous studies, our results exhibit a robust variation of τ_α with the
25 focal mechanism. These parameters are, on average largest for strike-slip earthquakes, followed by
26 normal-faulting events, with the lowest values for reverse earthquakes for hypocentral depths < 180
27 km. On the contrary, at depths in the range of 180 - 240 km, τ_α for reverse earthquakes is higher than
28 for normal-faulting events. Regarding the behavior of apparent stress with depth, our results agree with



29 the existence of a bimodal distribution with two depth intervals where the apparent stress is maximum
30 for normal-faulting earthquakes. Finite-fault energy estimations also support focal mechanism
31 dependence of apparent stress, but only for shallow earthquakes ($Z < 30$ km). The population of slip
32 distributions used was too small to conclude that finite-fault energy estimations support the dependence
33 of average apparent stress on rupture type at different depth intervals.

34

35 **1 Introduction**

36 The radiated seismic energy (E_R) is a crucial source parameter that accounts for the size of an
37 earthquake. The seismic energy is also a valuable parameter for understanding the dynamics of the
38 rupture, especially in the case of large and complex earthquake sources (Venkataraman and Kanamori,
39 2004a; Convers and Newman, 2011). The radiated seismic energy is considered the main contribution
40 to the total wave energy radiated by an earthquake (Boatwright and Choy, 1986). The most common
41 approach to calculating E_R requires the integration of radiated energy flux in velocity-squared
42 seismograms (Haskell, 1964; Thatcher and Hanks, 1973; Boatwright, 1980; Kanamori et al., 1993;
43 Boatwright and Choy, 1986; Singh and Ordaz, 1994; Choy and Boatwright, 1995; Pérez-Campos and
44 Beroza, 2001). In order to recover the E_R of an event, the seismic records have to be corrected for
45 propagation path and source effects such as attenuation, site effects, geometric spreading, radiation
46 pattern, and directivity. In calculating seismic energy, information on the Earth's structure is required
47 since E_R needs to be measured over a broad range of distances. Inaccurate information on the Earth's
48 structure results in uncertainties in energy estimations, particularly at higher frequencies
49 (Venkataraman and Kanamori, 2004a). Furthermore, previous studies showed that estimates of E_R
50 based on regional and teleseismic data might differ by as much as a factor of 10 for the same
51 earthquake (Singh and Ordaz, 1994).

52



53 Choy and Boatwright (1995) reported a focal mechanism dependence on E_R . Later this observation was
54 confirmed by Pérez-Campos and Beroza (2001), showing that the mechanism dependence is not as
55 strong as reported previously. The degree of dependence of seismic energy on the focal mechanism is
56 affected by several factors that bias the estimate (e.g., uncertainties in the corner frequency, geometrical
57 spreading, hypocentral depth, and focal mechanism) (Pérez-Campos and Beroza, 2001). This
58 dependence can be expressed in terms of the apparent stress ($\tau_\alpha = \mu E_R/M_0$, where μ is the rigidity, Wyss
59 and Brune, 1968), energy to moment ratio (E_R/M_0), or slowness parameter ($\Theta = \log_{10}(E_R/M_0)$, Newman
60 and Okal, 1998). Previous studies showed that strike-slip events have the highest apparent stress ($\tau_\alpha =$
61 0.70 MPa), followed by normal-faulting and thrust earthquakes with 0.25 and 0.15 MPa, respectively
62 (Pérez-Campos and Beroza, 2001). On the other hand, some authors have observed that E_R/M_0 ratio is
63 different for different types of earthquakes, particularly in subduction zones. For example, tsunami
64 earthquakes have the smallest E_R/M_0 ratio ($7 \times 10^{-7} - 3 \times 10^{-6}$), interplate and downdip events have a
65 slightly larger ratio ($5 \times 10^{-6} - 2 \times 10^{-5}$), and intraplate and deep earthquakes have E_R/M_0 ratios similar
66 to crustal earthquakes ($2 \times 10^{-5} - 3 \times 10^{-4}$) (Venkataraman and Kanamori, 2004a). The origin of the
67 focal mechanism dependence is unclear, but it has been proposed that the stress drop is the cause of this
68 dependence of the radiated seismic energy on the type of faulting (Pérez-Campos and Beroza, 2001).

69

70 Other approaches have also been used to calculate seismic energy, such as those based on finite-fault
71 models (Ide, 2002; Venkataraman and Kanamori, 2004b; Senatorski, 2014). Ide (2002) calculated the
72 radiated energy using an expression based on slip and stress on the fault plane. Energy estimates from
73 this method tend to be smaller by about a factor of 3 compared with the integrating far-field waveforms
74 method. Venkataraman and Kanamori (2004b) used a formula for the energy radiated seismically from
75 a finite source as a function of the time-dependent seismic moment $M_0(t)$ and the properties of the
76 medium. Here, the moment rate function derived from kinematic inversion is used to calculate the E_R .



77 On the other hand, Senatorski (2014) used an overdamped dynamics approximation for estimating the
78 radiated seismic energy. The accuracy of this method depends on the rupture history. This approach
79 provides two energy parameters: 1) The finite-fault overdamped dynamics approximation (E_O) and, 2)
80 the energy obtained from the averaged finite-fault model (E_U). In both cases, the seismic energy
81 depends on the slip, rupture time, and seismic moment. According to Senatorski (2014), in most cases,
82 the radiated seismic energy estimated by integrating digital seismic waveforms (E_R) is in the following
83 range: $E_U < E_R < E_O$. Several seismic energy observations have been calculated and compiled in
84 different catalogs in the last two decades. In this study, we reexamine the possible dependence of
85 seismic energy on the focal mechanism with an additional classification based on the type of rupture,
86 considering pure and oblique mechanisms separately. We also investigate the potential influence of
87 focal mechanism on the derived estimates of radiated seismic energy from finite-fault models.
88 Additionally, we explored the relationship between depth and the variables E_R/M_0 and τ_α . Furthermore,
89 we established conversion relationships between various types of energy estimates. These findings play
90 a crucial role in enhancing our understanding of the rupture processes associated with different types of
91 earthquakes.

92

93 **2 Data and methods**

94 **2.1 Data**

95 We retrieved and classified focal mechanism solutions from the global CMT catalog (Ekström et al.,
96 2012) using a ternary diagram based on the Kaverina et al. (1996) projection. This approximation
97 classifies focal mechanism into seven classes of earthquakes: 1) normal (N); 2) normal – strike-slip (N-
98 SS); 3) strike-slip – normal (SS-N); 4) strike-slip (SS); 5) strike-slip – reverse (SS-R); 6) reverse –
99 strike-slip (R-SS); and 7) reverse (R) (Fig. 1). For implementing fault-plane classification, we used the
100 software FMC developed by Álvarez-Gómez (2019). Additionally, we used radiated seismic energy



101 data and finite-fault models reported by the Incorporated Research Institutions for Seismology (IRIS)
102 and the United States Geological Survey (USGS), respectively. To have homogeneity in the analyzed
103 data, we do not include seismic energy observations and finite-fault models from other sources to avoid
104 bias. IRIS reported automated E_R solutions for global earthquakes with an initial magnitude above M_w
105 6.0. We studied 3331 events worldwide during the period April 1990 – October 2022 (Fig. 2). Results
106 include broadband energy solution (frequency band in the interval of 0.5 – 70 s) from vertical-
107 component seismograms recorded at teleseismic distances ($25^\circ \leq \Delta \leq 80^\circ$) (Convers and Newman,
108 2011; Hutko et al., 2017). Finite-fault models are determined with a kinematic inversion based on the
109 wavelet domain (Ji et al., 2002). The procedure jointly inverts body and surface waves on a fault plane
110 aligned with focal mechanism estimates from USGS W-phase or gCMT solutions. We used 231 finite-
111 fault models from 1990 to 2022 (Fig. 2). After classifying the events, we determined scaling
112 relationships for the reported seismic energies and analyzed the behavior of the E_R/M_0 ratio and τ_a . The
113 seismic energy was also determined using finite-fault models with the techniques described in the
114 following section to know if there is a difference in estimates related to the faulting type. Seismic
115 velocities and rock densities were taken from the ak135-F velocity model (Kennett et al., 1995;
116 Montagner and Kennett, 1995); rigidity was calculated as $\mu = \rho\beta^2$.

117

118 2.2 Methods

119 2.2.1 Radiated seismic energy derived from seismic waves

120 In the following, we described the procedure to calculate E_R implemented by IRIS. Radiated energies
121 used in this study were calculated with the method of Boatwright and Choy (1986) as implemented by
122 Convers and Newman (2011). Using velocity seismograms of the P -wave group (consisting of
123 $P+pP+sP$ phases), the energy is calculated at teleseismic distances. The seismic energy flux from the P -
124 wave group (ϵ_{gp}) is calculated from the velocity spectrum ($\dot{u}(\omega)$) as:



125

$$126 \quad \varepsilon_{gP} = \frac{\rho(z)\alpha(z)}{\pi} \int_0^{\infty} |\dot{u}(\omega)|^2 \exp(\omega t_{\alpha}^*) d\omega \quad , \quad (1)$$

127

128 where $\rho(z)$ and $\alpha(z)$ are the density and P -wave velocity at the source depth (z), and the exponential
129 term t_{α}^* corrects for anelastic attenuation. Subsequently, the energy flux is corrected for geometrical
130 spreading, radiation pattern, and partitioning between P and S waves. The radiated seismic energy at a
131 given station is calculated as:

132

$$133 \quad E_R^P = 4\pi \langle F^P \rangle^2 \left(\frac{R^P}{F^{gP}} \right)^2 \varepsilon_{gP} \quad , \quad (2)$$

134

135 where $\langle F^P \rangle^2$ is the mean radiation pattern coefficient for P -waves, R^P is the geometrical spreading
136 factor of P -waves, F^{gP} is the generalized radiation pattern coefficient for the P -wave group.

137

$$138 \quad (F^{gP})^2 = (F^P)^2 + (PPF^{pP})^2 + \frac{2\alpha(z)}{3\beta(z)} q (CSP F^{sP})^2 \quad , \quad (3)$$

139

140 where $\beta(z)$ is the S -wave velocity at the source depth, C is the correction for wavefront sphericity, F_p ,
141 F_{pP} , and F_{sP} are radiation pattern coefficients for the P , pP , and sP waves, respectively (Aki and
142 Richards, 1980). The parameter q represents the relative partitioning between S and P waves (using $q =$
143 15.6, Boatwright and Fletcher, 1984). PP and SP are the reflection coefficients for the pP and sP wave
144 phases at the free surface. Finally, the radiated seismic energy obtained from the P -wave or S -wave
145 groups can be estimated with the formulae $E_R = (1 + q)E_R^P = (1 + 1/q)E_R^S$. For each event, the final



146 assigned seismic energy is the average for all the stations used.

147

148 **2.2.2 Radiated energy estimations from finite-fault slip models**

149 Senatorski (2014) introduced a method to estimate energy parameters derived from kinematic slip

150 models. In this method, the radiated seismic energy is expressed in terms of slip velocities using an

151 overdamped dynamics approximation (Senatorski, 1994; 1995). The method provides two energy

152 parameters: 1) the overdamped dynamics energy approximation (E_O) and 2) the uniform model energy

153 estimation (E_U). The accuracy of the overdamped dynamics solutions depends on the rupture history.

154 Senatorski (2014) showed that in most cases, $E_U < E_R < E_O$. The energy parameter E_O is calculated as:

155

$$156 \quad E_O = \frac{1}{2\beta(z)} \sum_i M_0^i V^i, \quad (4)$$

157

158 where $\beta(z)$ is the shear wave velocity at the source depth and M_0^i is the seismic moment released at

159 the i -th fault segment. V^i is given by $V^i = D^i / t_R^i$, and D^i , and t_R^i are the slips and risetimes at the i -th

160 segment, respectively. The averaged finite-fault model estimation assumes uniform slip (\bar{D}), and

161 slip velocity ($V = \bar{D} / T$), so

162

$$163 \quad E_U = \frac{1}{2\beta(z)} M_0 V, \quad (5)$$

164

165 where M_0 is the total seismic moment, and T is the rupture duration.

166

167



168 2.2.3 Radiated energy estimates based on moment rate functions of slip models

169 The radiated seismic energy can also be calculated through moment rate functions of finite-fault
170 models (Haskell, 1964; Aki and Richards, 1980; Rudnicki and Freud, 1981; Venkataraman and
171 Kanamori, 2004b). By ignoring the contribution from *P*-waves, which accounts for less than 5 % of the
172 total radiated energy, the radiated energy derived from moment rate functions (E_{mrt}) can be written as
173 (Venkataraman and Kanamori, 2004b):

174

$$175 \quad E_{mrt} = \frac{1}{10 \pi \rho(z) \beta^5(z)} \int_0^{\infty} |\ddot{M}(t)_0|^2 dt \quad ,$$

176

177 where $\rho(z)$ and $\beta(z)$ are the density and *S*-wave velocity, respectively, at the source depth, and $\ddot{M}(t)_0$
178 is the derivative of the moment rate function ($\dot{M}_0(t)$) estimated from a finite-fault model.

179

180 3 Results

181 We used different methods to quantify the radiated seismic energy. Table 1 shows the calculated scaling
182 relationships for E_R for each energy method and type of faulting. Figs. 3, 4, 5, and 6 display the energy
183 scaling relations derived from the velocity flux integration (E_R), overdamped dynamics energy
184 approximation (E_O), the uniform model energy estimation (E_U), and moment rate function methods
185 (E_{mrt}), respectively. Our results showed some disparities in the calculated radiated seismic energies
186 obtained with different techniques or data types. When comparing E_R with the other methods to
187 estimate seismic energy, we find that the lowest average difference factors are for E_O estimates, ranging
188 from 0.28 to 0.77 (Fig. 7). Conversely, mean difference factors can be as high as 20 for E_U estimations
189 (Fig. 8). Average difference factors exhibit intermediate values for E_{mrt} calculations, fluctuating from
190 1.53 to 3.27 (Fig. 9). Regarding the rupture type, reverse earthquakes have the highest dispersion, but



191 they have the most significant number of observations (Figs. 7 to 9). Conversion relationships between
192 E_R and E_O , E_U , and E_{mrt} are presented in Table 2, which may be helpful when considering either method
193 of estimation.

194

195 In terms of the E_R/M_0 ratio, our results showed that SS, SS-N, and SS-R events have the highest mean
196 values ($3.06 \times 10^{-5} < E_R/M_0 < 3.75 \times 10^{-5}$) (Fig. 10). R-SS earthquakes have a slightly lower mean ratio
197 ($E_R/M_0 = 2.87 \times 10^{-5}$) (Fig. 10). Average E_R/M_0 ratio fluctuates from 2.31×10^{-5} to 2.37×10^{-5} for N-SS
198 and N events, respectively (Fig. 10). On the other hand, the lowest values of E_R/M_0 are related to R
199 earthquakes ($E_R/M_0 = 1.70 \times 10^{-5}$) (Fig. 10). Most of the rupture types present a differentiated behavior
200 of E_R/M_0 in terms of depth with the existence of two clusters, above and below about 300 km depth
201 (Fig. 11). In contrast, strike-slip earthquakes demonstrate a distinct pattern, with the majority of E_R/M_0
202 observations concentrated at depths shallower than 50 km (Fig. 11). Furthermore, at shallow depths, the
203 radiated energy-to-moment ratio shows large variability compared to observations of deep earthquakes
204 (Fig. 11).

205

206 Previous studies have provided evidence that mean τ_α estimates can be obtained using regression
207 models, specifically through the equation $\log_{10} E_R = \log_{10} M_0 + b$ with $\tau_\alpha = \mu 10^b$, supporting the focal
208 mechanism dependence of E_R (Choy and Boatwright, 1995; Pérez-Campos and Beroza, 2001). To test
209 that this dependence persists with depth, we conducted regressions every 30 km of depth considering
210 variations of μ and at least ten observations. First, we evaluated reported seismic energy observations
211 based on the velocity flux integration method (Table 3). Our results for average apparent stress agree
212 with previous studies where τ_α follows the following behavior (R-SS, R) < (N-SS, N) < (SS, SS-N, SS-
213 R) in the range of 0 – 180 km (Table 3). On the contrary, τ_α is higher for R events than for N
214 earthquakes at depths from 180 to 240 km (Table 3). At depths higher than 240 km, only N events were



215 obtained under the assumptions considered. In Table 3, we summarized results for all the depth
216 intervals showing the mean values and their 95% log-normal geometric spread.

217

218 Our results also showed that N and N-SS events exhibit a bimodal distribution of τ_α with depth (Fig.
219 12). The most significant values of τ_α occur in two depth ranges of approximately 40 – 60 km and 580 –
220 650 km, where maximum apparent stresses approach 8 and 16 MPa, respectively (Fig. 12). N-SS, R, R-
221 SS, SS-N, and SS-R events also showed two maximum values of τ_α ranging from 7 to 11 MPa and 9 to
222 15 MPa for shallow and deep earthquakes, respectively (Fig. 12). For SS events, there is only one depth
223 range over which τ_α for strike-slip earthquakes shows maxima. In this case, the highest values of τ_α are
224 found in the deeper depth range from 50 to 100 km ($\tau_\alpha \sim 12$ MPa) (Fig. 12). On the other hand, the
225 average apparent stress estimates based on the finite-fault models exhibit a similar dependence on the
226 focal mechanism than those obtained with the velocity flux integration method at shallow depths ($Z <$
227 30 km) (Table 4). Regressions showed that τ_α follows the following behavior $R < N < (SS, SS-R)$ for E_U
228 and E_{mrt} estimations (Table 4). In contrast, E_O showed no clear dependence of τ_α with the focal
229 mechanism (Table 4). Due to the constraint of at least ten observations (slip distributions) for each 30
230 km depth interval, we could not analyze the dependence of τ_α on the type of faulting at a deeper depth.

231

232 **4 Discussion**

233 In this study, we analyzed radiated seismic energy and parameters that measure the amount of energy
234 per unit of the moment, such as the apparent stress and the energy-to-moment ratio (also known as
235 scaled energy or apparent strain), considering their respective particularities. The advantage of using τ_α
236 is that it can be related to other stress processes associated with the seismic rupture, such as the stress
237 drop. On the other hand, many finite-fault models of the spatiotemporal slip history for moderate and
238 large earthquakes exist. From these models, important information can be extracted, such as fault



239 dimensions (Mai and Beroza, 2000), static stress drop (Ripperger and Mai, 2004), or radiated seismic
240 energy (Ide, 2002; Senatorski, 2014). When using finite-fault models to determine E_R , it is necessary to
241 consider that they usually explain low-frequency seismic waves. However, the higher-frequency wave
242 contribution is necessary for calculating the total radiated seismic energy. This issue brings differences
243 among finite-fault energy estimates and those from integrating far-field waveforms.

244

245 Furthermore, finite-fault seismic energy estimations are strongly affected by event location, the number
246 of available data, faulting parameterization, and velocity structure. The degree of discrepancy between
247 the finite-fault energy estimates (E_{mrt} , E_O , and E_U) with respect to the velocity flux integration method
248 (E_R) is variable among the different types of seismic energy. For example, the moment rate functions
249 are relatively robustly determined by teleseismic data, while rupture dimensions are strongly affected
250 by model parameters (Ye et al., 2016). This may explain why the average difference factor (E_R/E_U) is
251 greater than the E_R/E_{mrt} factor (Figs. 8 and 9). Another source of discrepancies in finite-fault energy
252 calculations comes from the spatial and temporal smoothing in resolving the kinematic slip distribution
253 and the rupture velocity assigned. Errors associated with the assumptions are tough to quantify as they
254 propagate into the energy estimates in complex ways.

255

256 Our results agree with previous estimates of E_O and E_U , confirming that $E_R \in (E_U, E_O)$ for most
257 earthquakes. The overdamping approximation (E_O) can be used to characterize the heterogeneity of the
258 rupture process. Senatorski (2014) states that if the ratio E_O/E_R is < 0.4 , the rupture can be represented
259 as a simple dislocation rupture. $E_O/E_R > 1$ is expected in the case of heterogeneous rupture processes.
260 On the other hand, some of the suggested explanations for the observation that $E_O > E_R$ are: 1) the
261 finite-fault slip models require refinement; 2) the seismic energy estimations require correction for
262 directivity, modified attenuation factors, or sites effects; and 3) some other factors are not considered in



263 the calculations such as the fact that the energy dissipation is not taken into account by the planar faults
264 (Senatorski, 2014).

265

266 The radiated seismic energy scaled by seismic moment is an essential characterization of earthquake
267 dynamics. The low E_R/M_0 of reverse events is associated with tsunami events being compatible with the
268 results of previous studies (Newman and Okal, 1998; Venkataraman and Kanamori, 2004a; Convers
269 and Newman, 2011; Ye et al., 2016). Our results showed that E_R/M_0 has a large scatter from 6×10^{-7} to 2
270 $\times 10^{-4}$ for all the rupture types, but no evident magnitude dependence (Fig. 10). One of the reasons for
271 the dispersion of E_R/M_0 is that it depends on many seismogenic properties of the source region (Fig.
272 10). As a consequence, E_R/M_0 varies significantly in different tectonic environments and deep
273 conditions such as pressure and temperature (Fig. 11). Even within the same tectonic environment,
274 E_R/M_0 has significant variations, as has been reported by Plata-Martínez et al. (2019) in the Middle
275 American Trench, where variations in E_R/M_0 are associated with heterogeneities along the trench, such
276 as asperities patches. The different types of earthquakes have differences in the frequency content of
277 the seismic energy released.

278

279 Venkataraman and Kanamori (2004a) reported that E_R/M_0 is in the range of $5 \times 10^{-6} - 2 \times 10^{-5}$ for
280 interplate and downdip earthquakes, which are mainly consistent with reverse and normal faulting. Our
281 results showed that the average values of E_R/M_0 for R and N events are 1.70×10^{-5} and 2.37×10^{-5} ,
282 respectively, and both values are within the interval defined by Venkataraman and Kanamori (2004a).
283 The E_R/M_0 ratio for deep earthquakes varies from 2.0×10^{-5} to 3.0×10^{-4} (Venkataraman and Kanamori,
284 2004a). We found that E_R/M_0 for deep earthquakes of all types of rupture is in the interval of $2 \times 10^{-6} -$
285 2×10^{-4} but with a predominance of $1.0 \times 10^{-5} > E_R/M_0$ (Fig. 11). Despite the E_R/M_0 scatter, our results
286 depict a general trend for the average values of E_R/M_0 , which can be expressed as R < (N, N-SS, R-SS)



287 $< (SS, SS-R, SS-N)$ (Fig. 10), a similar tendency was reported by Convers and Newman (2011) where

288 E_R/M_0 follows $R < N < SS$.

289

290 Our results support the previously reported focal mechanism dependence of E_R (Choy and Boatwright,
291 1995; Pérez-Campos and Beroza, 2001; Convers and Newman, 2011) but narrow the range.

292 Examination of mean τ_α with various focal mechanisms and at different depths has been done for
293 different earthquake sizes and tectonic settings. We identified the largest values of apparent stress for

294 strike-slip events, intermediate values for normal-faulting events, and lowest for reverse-faulting events

295 in the depth interval of 0 – 180 km (Table 3). On the other hand, our results showed that at depths

296 between 180 and 240 km, τ_α for reverse earthquakes is higher than for normal-faulting events. This can

297 be explained, for example, in subduction zones, deep reverse earthquakes occur in the lower part of the

298 slab, where they are subjected to significantly large compressive stresses. A precise characterization of

299 the depth dependence of τ_α remains unclear at depths greater than 240 km. In Table 3, we present and

300 compare our results for τ_α , supporting the observation of the dependence of E_R on the type of faulting.

301 The origin of this focal dependence is unclear, but it has been raised that it reflects a mechanism-

302 dependent difference in stress drop (Pérez-Campos and Beroza, 2001). It can be highlighted with an

303 alternative definition for the apparent stress assuming that the dynamic and static stress drops are

304 roughly equivalent. Then τ_α can be expressed as $\tau_\alpha = (\eta_R \Delta\sigma)/2$, where η_R is the seismic efficiency, and

305 $\Delta\sigma$ is the stress drop (Convers and Newman, 2011). Allmann and Shearer (2009) provided additional

306 information to support the role of stress drop on the dependency of apparent stress with the type of

307 faulting. They found a dependence of median stress drop on the focal mechanism with a factor of 3–5

308 times higher stress drops for strike-slip events and two times higher stress drops for intraplate events

309 compared to interplate events.

310



311 Nevertheless, other interpretations of the apparent stress variation are related to the mechanical
312 properties of the rock, such as the reduction of rigidity in shallow subduction environments or
313 increment in lithostatic pressure if no change in regional rigidity is assumed (Convers and Newman,
314 2011). In fact, the variation of such estimates concerning expected spatial variations in rigidity is an
315 issue that still needs attention. Choy and Kirby (2004) also suggested that τ_{α} can be related to fault
316 maturity. For example, lower stress drops are needed to reach rupture in mature faults. On the contrary,
317 earthquakes generated at immature faults (low cumulative displacement) radiate more energy per unit
318 of seismic moment. Regarding the behavior of τ_{α} with depth, our results agree with the existence of a
319 bimodal distribution with two depth intervals where the apparent stress is maximum for normal-
320 faulting earthquakes, as reported by Choy and Kirby (2004). We also found that almost all types of
321 faulting (SS-N, SS-R, R-SS, R, N-SS, and N) show two depth ranges where the stress is maximum, but
322 in the case of normal-faulting earthquakes, it is very well defined. On the other hand, almost all strike-
323 slip earthquakes show a single interval of depths where the apparent stress is maximum (Fig. 12).
324 Earthquakes with an oblique focal mechanism show a mixed behavior of τ_{α} , as is the case of the SS-N
325 and SS-R events that present similar characteristics to normal and reverse earthquakes in terms of the
326 depth distribution of τ_{α} .

327

328 In terms of the spatial distribution of E_R and τ_{α} (Figs. S1 to S14), the highest values of τ_{α} for N events
329 are located at the border between the Nazca and South American plates, the Eurasian and Philippine
330 plates, the Indo-Australian and Pacific plates, the Philippine and Pacific plates, and the Pacific and
331 North American plates (in the Alaska region) (Fig. S1). Regarding the seismic energy of earthquakes,
332 the regions where the most energetic earthquakes have occurred concur with the aforementioned areas,
333 with the addition of the border between the Cocos and North American plates (Fig. S2). The high τ_{α}
334 normal-faulting events are associated with regions of intense deformation, such as a sharp slab bending



335 or zones where opposing slabs collide (Choy and Kirby, 2004). At shallow depths ($Z < 35$ km), high- τ_{α}
336 events are related to the beginning of the subduction beneath the overriding plate (Choy and Kirby,
337 2004). Our results support the observation that the average apparent stress of intraslab normal-faulting
338 events is considerably higher than the average τ_{α} of interplate thrust-faulting earthquakes reported by
339 Choy and Kirby (2004) (Figs. S1 and S5).

340

341 In the case of R earthquakes, the highest values of E_R and τ_{α} are in the limit of the Eurasian and
342 Philippine plates, the Nazca and South American plates, the Philippine and Pacific plates, the Indo-
343 Australian and Pacific plates, and, the Eurasian and Indo-Australian plates (Figs. S5 and S6). In
344 contrast, strike-slip events with the highest values of E_R and τ_{α} are on the border between the African
345 and Eurasian plates (in Türkiye), the Eurasian and Indo-Australian plates, the Philippine and Eurasian
346 plates, the Indo-Australian and Pacific plates (in New Zealand), and the Caribbean and South American
347 plates (Figs. S13 and S14). We have found that several SS earthquakes are located in the oceanic
348 lithosphere at depths < 50 km. Many of the SS events with high τ_{α} are located near the plate-boundary
349 triple junctions where there are high rates of intraplate deformation, as previously reported by Choy
350 and McGarr (2002).

351

352 Finally, when using seismic energy estimates based on finite-fault models (E_O and E_{mfr}), a clear
353 dependence of the average apparent stress with the focal mechanism is observed at shallow depths ($Z <$
354 30 km) (Table 4). For example, using E_U and E_{mfr} , the average τ_{α} follows $R < N < (SS-R, SS)$. If E_O is
355 used, the mean apparent stress exhibits similar values for SS-R, N, and R events (Table 4). However,
356 the lack of a significant number of observations for some types of earthquakes makes it challenging to
357 evaluate the use of finite-fault models to determine apparent stress. Despite these limitations, the
358 methods used to estimate the seismic energy based on finite-fault models are a quick alternative to



359 calculate a range of energy variation once a slip distribution is obtained.

360

361 **5 Conclusion**

362 We studied the radiated seismic energy, energy-to-moment ratio, and apparent stress for a different type
363 of faulting. Our data relies on different methodologies employing the velocity flux integration and
364 finite-fault models to determine the seismic energy. The approach based on slip distributions involved
365 the utilization of two techniques: 1) total moment rate functions and 2) overdamped dynamics
366 approximation. We analyzed 3331 energy observations derived from integrating far-field waveforms.
367 On the other hand, we used 231 finite-fault models. The energy estimates are consistent with each
368 other, with the maximum average difference factor for E_U estimates followed by E_{mt} and E_O ,
369 respectively. The estimated energy differences are within the margin reported in the literature, which
370 can reach a factor higher than 10. The methods used to estimate seismic energy based on finite fault
371 models are an easily implemented alternative that gives results compatible with the seismic record
372 integration technique, given the larger uncertainties of these methods. We also derived scaling
373 relationships for the different types of energies and conversion relations.

374

375 In terms of the behavior of the E_R/M_0 ratio, our results showed a high scatter without a clear
376 dependence on magnitude. Like previous studies, we observe a robust variation of E_R/M_0 with the type
377 of faulting, which can be expressed as $R < (N, N-SS, R-SS) < (SS, SS-R, SS-N)$. Our E_R/M_0 estimates
378 for deep earthquakes are also consistent with reported values. By analyzing the average apparent stress,
379 our results also support the previously reported focal mechanism dependence of E_R at depths ranging
380 from 0 to 180 km. We found that normal-faulting events have intermediate values of τ_α between strike-
381 slip and reverse events using the energy flux integration approach in agreement with previous studies.
382 On the other hand, τ_α for reverse earthquakes is higher than for normal-faulting events at depths



383 between 180 and 240 km. In contrast, a clear focal mechanism dependence is observed when finite-
384 fault methods are used to estimate the mean apparent stress at shallow depths ($Z < 30$ km). This study's
385 population of slip distributions was too small to conclude that finite-fault energy estimations support
386 the mechanism dependence of average apparent stress at different depths. There are two depth ranges
387 over which apparent stress for SS-N, SS-R, R-SS, R, N-SS, and N earthquakes shows maxima.
388 Earthquakes with an oblique focal mechanism show a mixed behavior of energy parameters since it has
389 common characteristics of two types of faults; in some cases, one of them predominates over the other.

390

391 Code availability. Generic Mapping Tools (GMT5) is available at <http://gmt.soest.hawaii.edu/>, last
392 access: 19 June 2023. FMC is available at <https://github.com/Jose-Alvarez/FMC>, last access: 19 June
393 2023.

394

395 Data availability. Radiated seismic energy data are acquired from the IRIS Data Services Products:
396 EQEnergy (<https://ds.iris.edu/ds/products/eqenergy/>). Focal mechanisms are taken from Global CMT
397 catalog (<https://www.globalcmt.org/>). Finite-fault models are acquired from the USGS earthquake
398 catalog (<https://earthquake.usgs.gov/earthquakes/search/>).

399

400 Author contributions. QRP designed the idea, developed the methodology and performed the
401 preliminary analyses. QRP and FRZ discussed and analyzed the results and wrote the paper.

402

403 Competing interests. The authors declare that they have no conflict of interest.

404

405 Acknowledgments. Quetzalcoatl Rodríguez-Pérez was supported by the Mexican National Council for
406 Science and Technology (CONACYT) (Cátedras program - project 1126).



407

408 Financial support. This research has been supported by the CONACYT (grant no. Catedras program,
409 project 1126).

410

411 **References**

412 Aki, K., Richards, P.G.: Quantitative seismology, 913 pp., W. H. Freeman, New York, 1980.

413

414 Allmann, B., Shearer, P.M.: Global variations of stress drop for moderate to large earthquakes, J.
415 Geophys. Res., 114, B01310, <https://doi.org/10.1029/2008JB005821>, 2009.

416

417 Álvarez-Gómez, J.A.: FMC-Earth focal mechanisms data management, cluster and classification,
418 Software X 9, 299-307, <https://doi.org/10.1016/j.softx.2019.03.008>, 2019.

419

420 Boatwright, J.L.: A spectral theory for circular seismic sources; simple estimates of source dimension,
421 dynamic stress drop, and radiated seismic energy, Bull. Seism. Soc. Am., 70, 1-27,
422 <https://doi.org/10.1785/BSSA0700010001>, 1980.

423

424 Boatwright, J.L., Fletcher, J.B.: The partition of radiated energy between *P* and *S* waves, Bull. Seism.
425 Soc. Am., 74, 361-376, <https://doi.org/10.1785/BSSA0740020361>, 1984.

426

427 Boatwright, J.L., Choy, G.L.: Teleseismic estimates of the energy radiated by shallow earthquakes, J.
428 Geophys. Res., 91, 2095-2112, <https://doi.org/10.1029/JB091iB02p02095>, 1986.

429

430 Choy, G.L., Boatwright, J.L.: Global patterns of radiated seismic energy and apparent stress, J.



431 Geophys. Res 100, B9, 18205-18228, <https://doi.org/10.1029/95JB01969>, 1995.

432

433 Choy, G.L., McGarr, A.: Strike-slip earthquakes in the oceanic lithosphere: observations of
434 exceptionally high apparent stress, Geophys. J. Int., 150, 506-523, <https://doi.org/10.1046/j.1365-246X.2002.01720.x>, 2002.

436

437 Choy, G.L., Kirby, S.H.: Apparent stress, fault maturity and seismic hazard for normal-fault
438 earthquakes at subduction zones, Geophys. J. Int., 159, 991-1012, <https://doi.org/10.1111/j.1365-246X.2004.02449.x>, 2004.

440

441 Convers, J.A., Newman, A.V.: Global evaluation of large earthquake energy from 1997 through mid-
442 2010, J. Geophys. Res., 116, B08304, <https://doi.org/10.1029/2010JB007928>, 2011.

443

444 Ekström, G., Nettles, M., Dziewoński, A.M.: The global CMT project 2004–2010: Centroid-moment
445 tensors for 13,017 earthquakes, Phys. Earth Planet. Inter., 201-201, 1-9,
446 <https://doi.org/10.1016/j.pepi.2012.04.002>, 2012.

447

448 Haskell, N.A.: Total energy and energy spectral density of elastic wave radiation from propagating
449 faults, Bull. Seism. Soc. Am., 54, 1811-1841, <https://doi.org/10.1785/BSSA05406A1811>, 1964.

450

451 Hutko, A.R., Bahavar, M., Trabant, C., Weekly, R.T., Van Fossen, M., Ahern, T.: Data Products at the
452 IRIS-DMC: Growth and Usage, Seismol. Res. Lett., 88, 892-903, <https://doi.org/10.1785/0220160190>,
453 2017.

454



455 Ide, S.: Estimation of radiated energy of finite-source earthquake modes, *Bull. Seism. Soc. Am.*, 92,
456 2994-3005, <https://doi.org/10.1785/0120020028>, 2002.

457

458 Ji, C., Wald, D.J., Helmberger, D.V.: Source description of the 1999 Hector Mine, California
459 earthquake; Part I: Wavelet domain inversion theory and resolution analysis, *Bull. Seism. Soc. Am.*, 92,
460 1192-1207, <https://doi.org/10.1785/0120000916>, 2002.

461

462 Kanamori, H., Mori, J., Hauksson, E., Heaton, T.H., Hutton, L.K., Jones, L.M.: Determination of
463 earthquake energy release and M_L using terrascope, *Bull. Seismol. Soc. Am.*, 83, 330-346,
464 <https://doi.org/10.1785/BSSA0830020330>, 1993.

465

466 Kaverina, A.N., Lander, A.V., Prozorov, A.G.: Global creepex distribution and its relation to
467 earthquake-source geometry and tectonic origin, *Geophys. J. Int.*, 125, 249-265,
468 <https://doi.org/10.1111/j.1365-246X.1996.tb06549.x>, 1996.

469

470 Kennett, B.L.N., Engdahl, E.R., Buland, R.: Constraints on seismic velocities in the earth from travel
471 times, *Geophys. J. Int.*, 122, 108-124, <https://doi.org/10.1111/j.1365-246X.1995.tb03540.x>, 1995.

472

473 Mai, P.M., Beroza, G.C.: Source scaling properties from finite-fault-rupture models, *Bull. Seismol.*
474 *Soc. Am.*, 90, 604-615, <https://doi.org/10.1785/0119990126>, 2000.

475

476 Montagner, J.P., Kennett, B.L.N.: How to reconcile body-wave and normal-mode reference Earth
477 models?", *Geophys. J. Int.*, 125, 229-248, <https://doi.org/10.1111/j.1365-246X.1996.tb06548.x>, 1995.

478



479 Newman, A.V., Okal, E.A.: Teleseismic estimates of radiated seismic energy: the E/M_0 discriminant for
480 tsunami earthquakes, *J. Geophys. Res.*, 103, 26885-26898, <https://doi.org/10.1029/98JB02236>, 1998.

481

482 Pérez-Campos, X., Beroza, G.C.: An apparent mechanism dependence of radiated seismic energy, *J.*
483 *Geophys. Res.*, 106, B6, 11127-11136, <https://doi.org/10.1029/2000JB900455>, 2001.

484

485 Plata-Martínez, R., Pérez-Campos, X., Singh, S.K.: Spatial distribution of radiated seismic energy of
486 three aftershocks sequences at Guerrero, Mexico, subduction zone, *Bull. Seismol. Soc. Am.*, 109, 2556-
487 2566, <https://doi.org/10.1785/0120190104>, 2019.

488

489 Ripperger, J., Mai, P.M.: Fast computation of static stress changes on 2D faults from final slip
490 distributions, *Geophys. Res. Lett.*, 31, L18610, <https://doi.org/10.1029/2004GL020594>, 2004.

491

492 Rudnicki, J.W., Freund, L.B.: On energy radiation from seismic sources, *Bull. Seismol. Soc. Am.*, 71,
493 583-595, <https://doi.org/10.1785/BSSA0710030583>, 1981.

494

495 Senatorski, P.: Spatio-temporal evolution of faults: deterministic model, *Physica D*, 76, 420-435,
496 [https://doi.org/10.1016/0167-2789\(94\)90049-3](https://doi.org/10.1016/0167-2789(94)90049-3), 1994.

497

498 Senatorski, P.: Dynamics of a zone of four parallel faults: a deterministic model, *J. Geophys. Res.*, 100,
499 B12, 24111-24120, <https://doi.org/10.1029/95JB02624>, 1995.

500

501 Senatorski, P.: Radiated energy estimations from finite-fault earthquake slip models, *Geophys. Res.*
502 *Lett.*, 41, 3431-3437, <https://doi.org/10.1002/2014GL060013>, 2014.



503

504 Singh, S.K., Ordaz, M.: Seismic energy release in Mexican subduction zone earthquakes, Bull.

505 Seismol. Soc. Am., 84, 1533-1550, <https://doi.org/10.1785/BSSA0840051533>, 1994.

506

507 Thatcher, W., Hanks, T.C.: Source parameters of southern California earthquakes, J. Geophys. Res., 78,

508 8547-8576, <https://doi.org/10.1029/JB078i035p08547>, 1973.

509

510 Venkataraman, A., Kanamori, H.: Observational constraints on the fracture energy of subduction zone

511 earthquakes, J. Geophys. Res., 109, B05302, <https://doi.org/10.1029/2003JB002549>, 2004a.

512

513 Venkataraman, A., Kanamori, H.: Effect of directivity on estimates of radiated seismic energy, J.

514 Geophys. Res., 109, B04301, doi:10.1029/2003JB002548, <https://doi.org/10.1029/2003JB002548>,

515 2004b.

516

517 Wyss, M., Brune, J.N.: Seismic moment, stress, and source dimensions for earthquakes in the

518 California-Nevada region, J. Geophys. Res., 73, 4681-4694, <https://doi.org/10.1029/JB073i014p04681>,

519 1968.

520

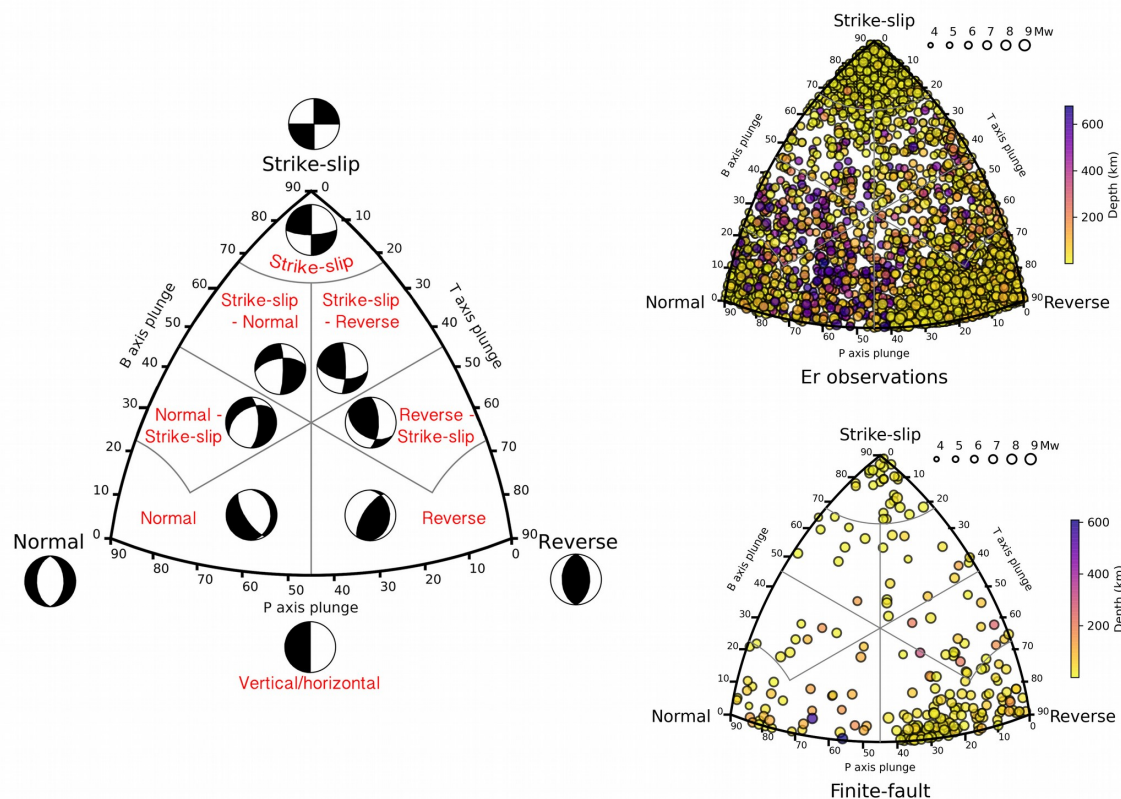
521 Ye, L., Lay, T., Kanamori, H., Rivera, L.: Rupture characteristics of major and great ($M_w \geq 7.0$)

522 megathrust earthquakes from 1990 to 2015: 1. Source parameter scaling relationships, J. Geophys.

523 Res., 121, 826-844, <https://doi.org/10.1002/2015JB012426>, 2016.

524

525



526

527

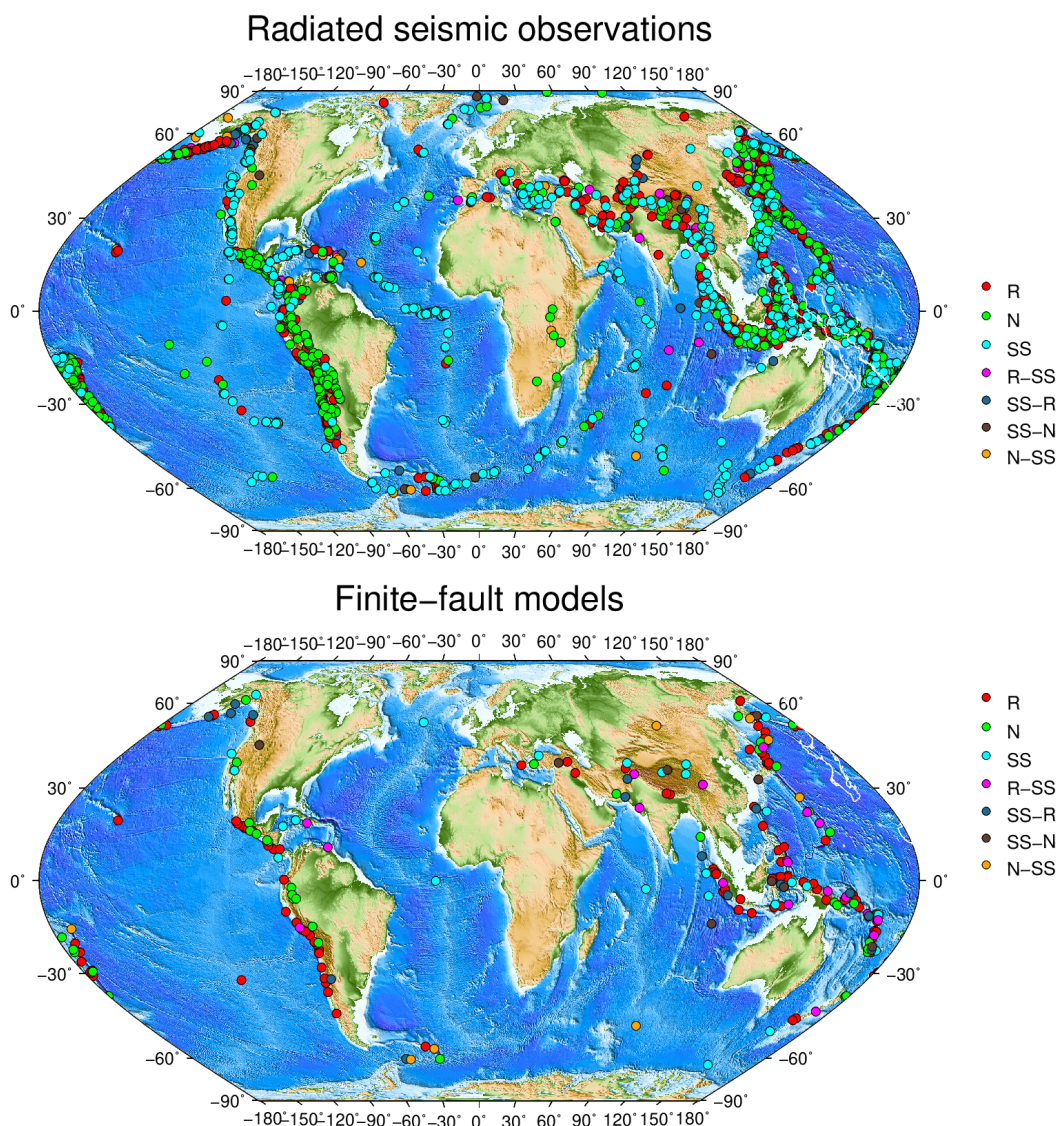
528 **Figure 1.** The Kaverina fault classification ternary diagram used to classify focal mechanisms (left
529 panel). Focal mechanisms are denoted by circles filled to indicate event depth in km, and the size of the
530 circle indicates the moment magnitude of the earthquake (right panels). The upper right panel shows
531 the rupture type of seismic events with a radiated seismic energy estimation. Rupture type of seismic
532 events with a finite-fault model used to estimate the radiated energy (lower right panel).

533

534

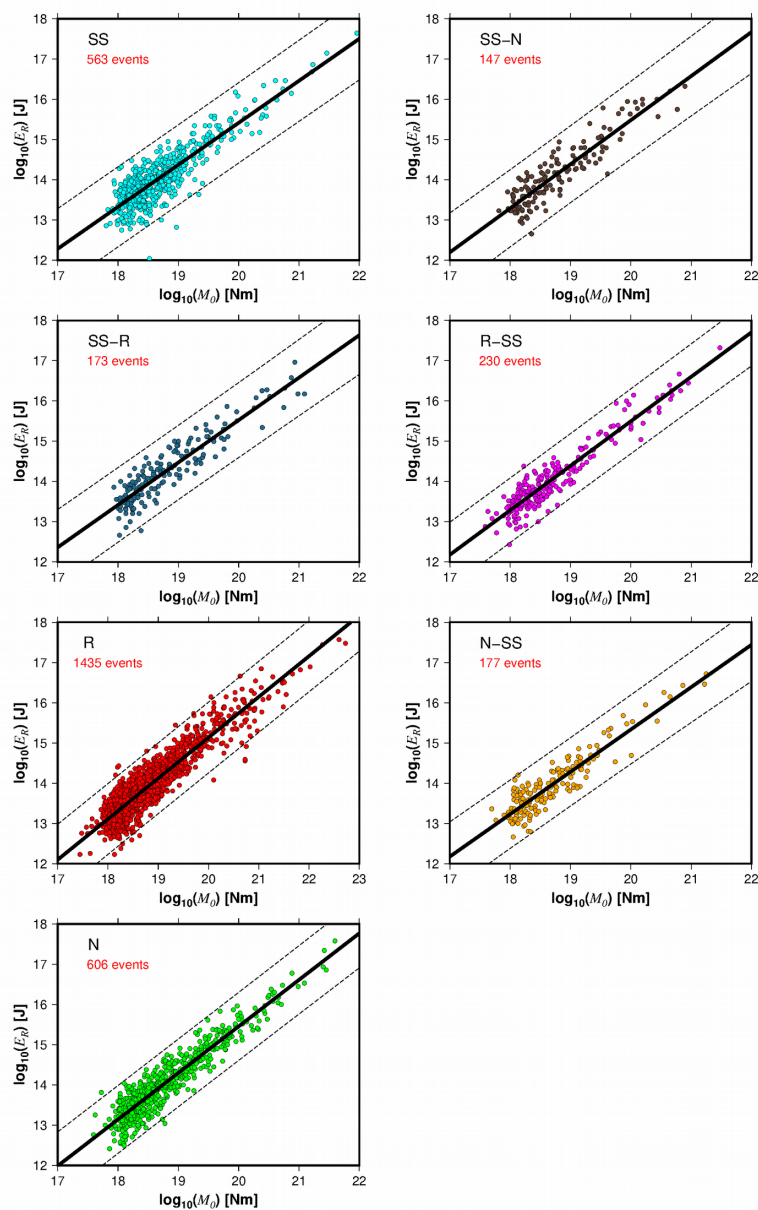
535

536



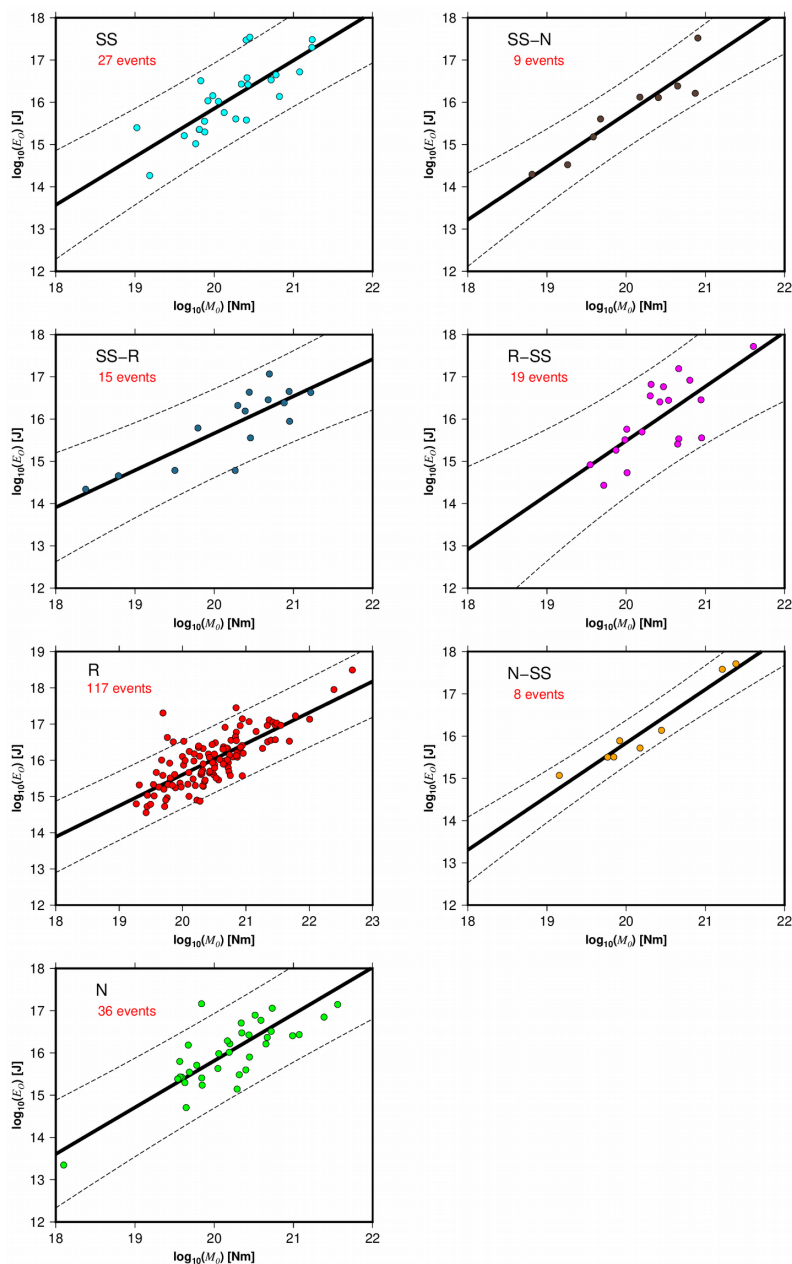
537

538 **Figure 2.** Hypocenter location and rupture type classification of earthquakes with reported radiated
539 seismic energy (E_R) (upper panel). Hypocenter location and rupture type classification of earthquakes
540 with a finite-fault model used to calculate the radiated seismic energy (E_R) (lower panel). R, reverse; R-
541 SS, reverse-strike-slip; SS, strike-slip; SS-R, strike-slip-reverse; SS-N, strike-slip-normal; N, normal;
542 and N-SS, normal-strike-slip.



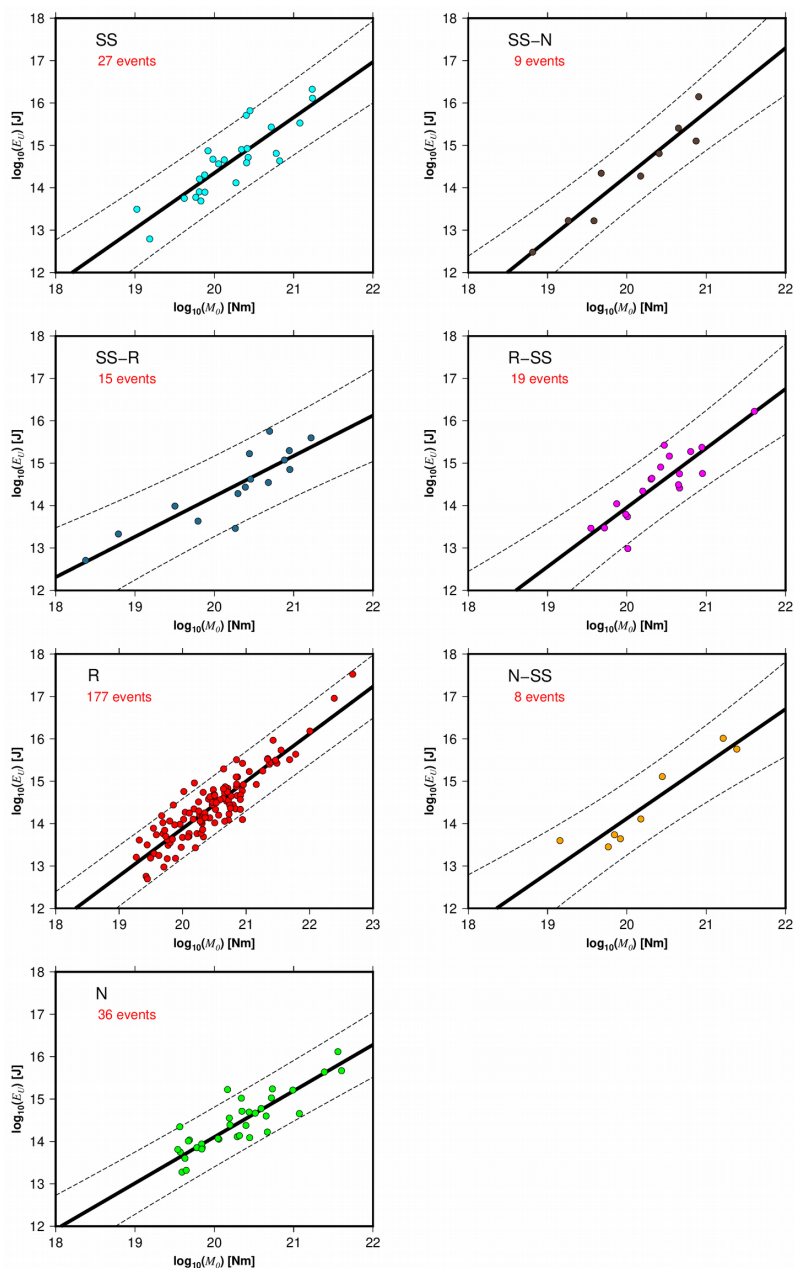
543

544 **Figure 3.** The radiated seismic energy (E_R) as a function of the seismic moment (M_0) for the different
545 rupture types. The solid black lines represent the best fit, and the dashed lines indicate the 95%
546 confidence interval about the regression lines.



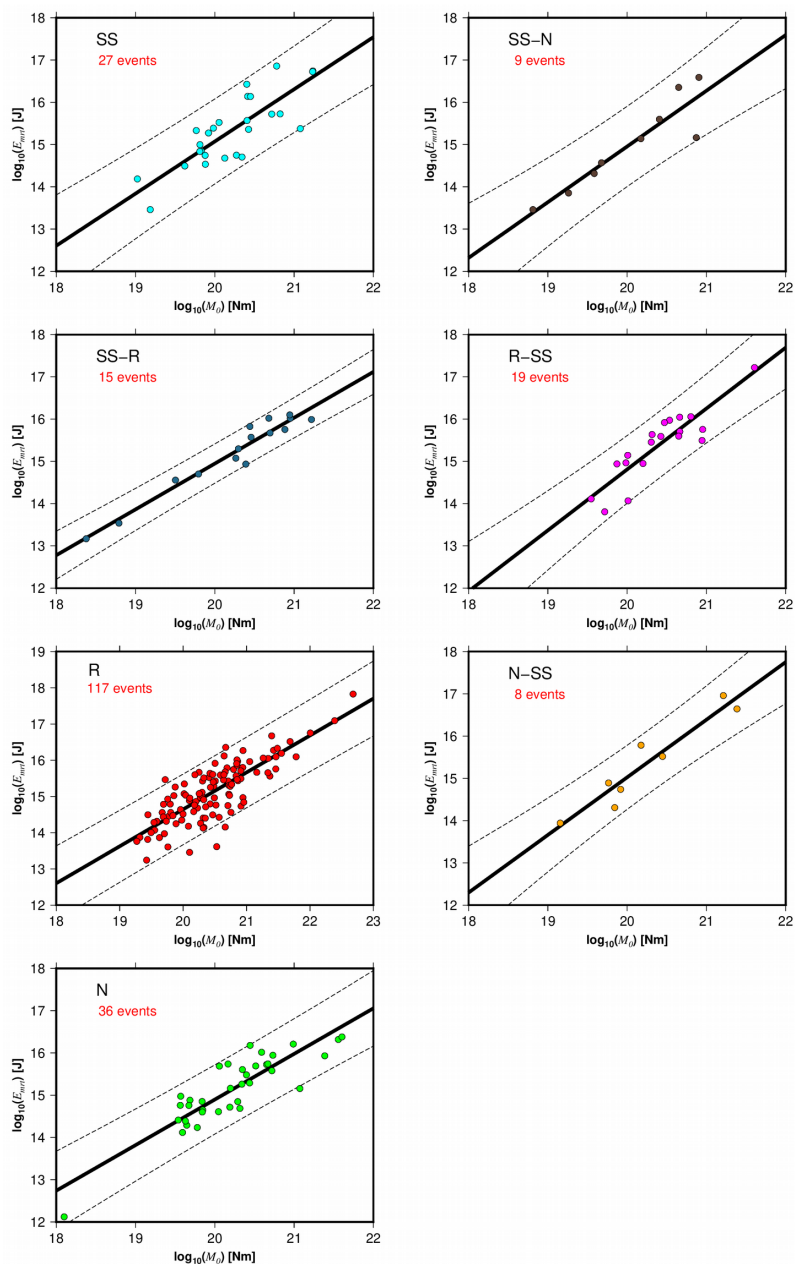
547

548 **Figure 4.** The overdamped dynamics approximation of the radiated energy (E_0) as a function of the
 549 seismic moment (M_0) for the different rupture types. The solid black lines represent the best fit, and the
 550 dashed lines indicate the 95% confidence interval about the regression lines.



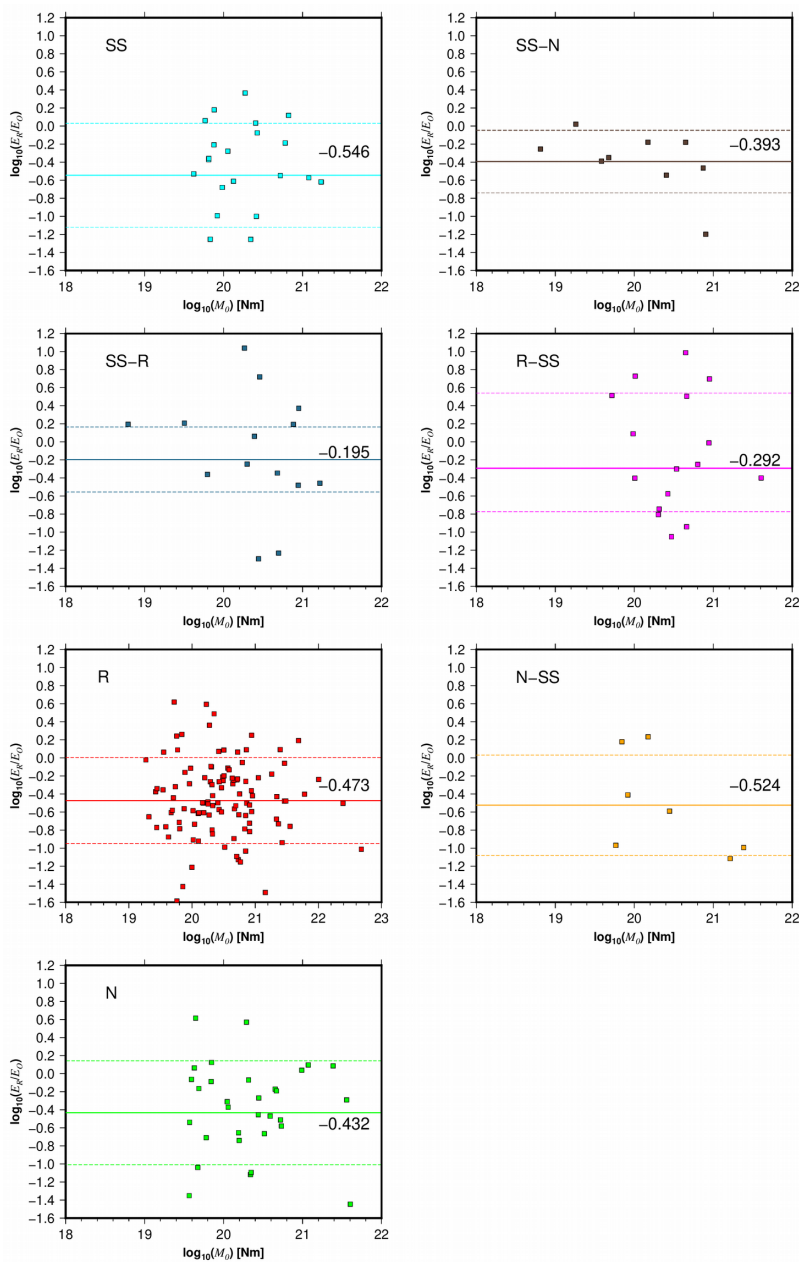
551

552 **Figure 5.** The energy obtained from the averaged finite-fault model (E_U) as a function of the seismic
 553 moment (M_0) for the different rupture types. The solid black lines represent the best fit, and the dashed
 554 lines indicate the 95% confidence interval about the regression lines.



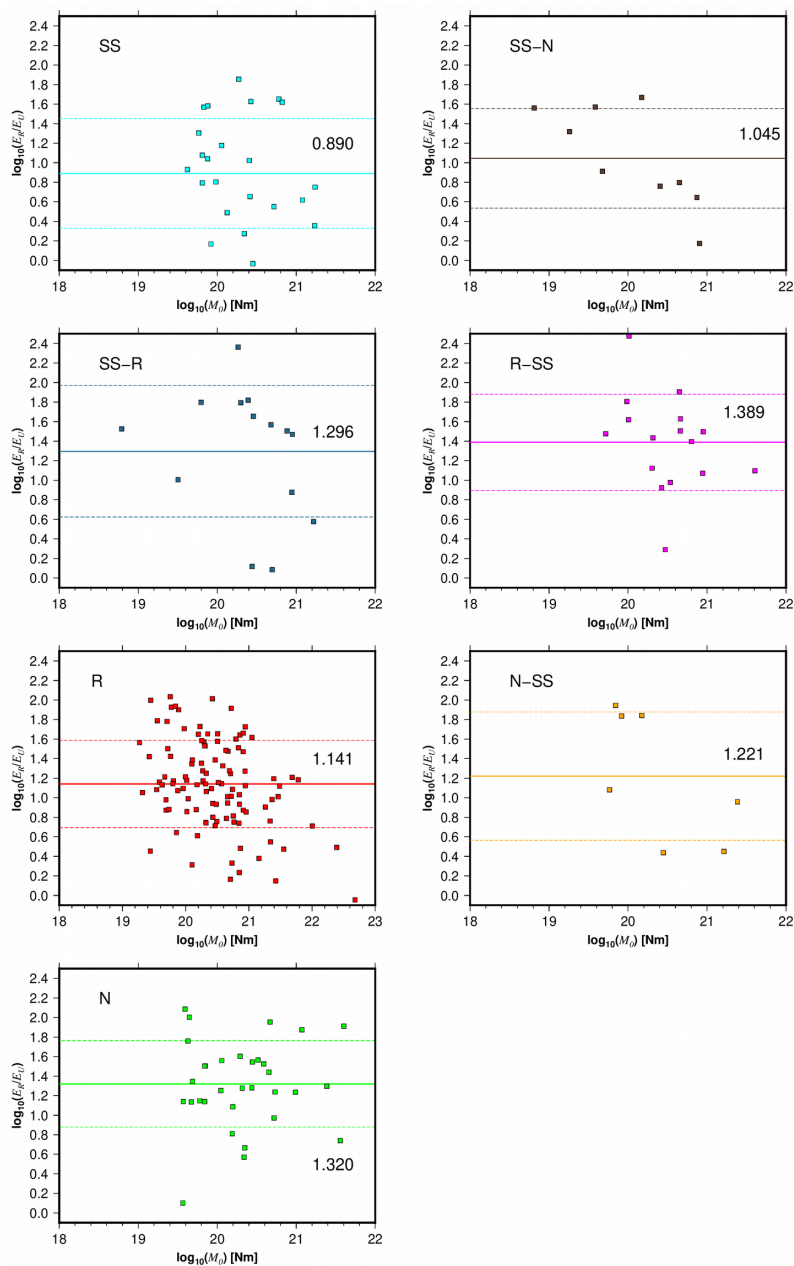
555

556 **Figure 6.** The radiated seismic energy based on moment rate functions (E_{mt}) versus seismic moment
557 (M_0) for the different rupture types. The solid black lines represent the best fit, and the dashed lines
558 indicate the 95% confidence interval about the regression lines.



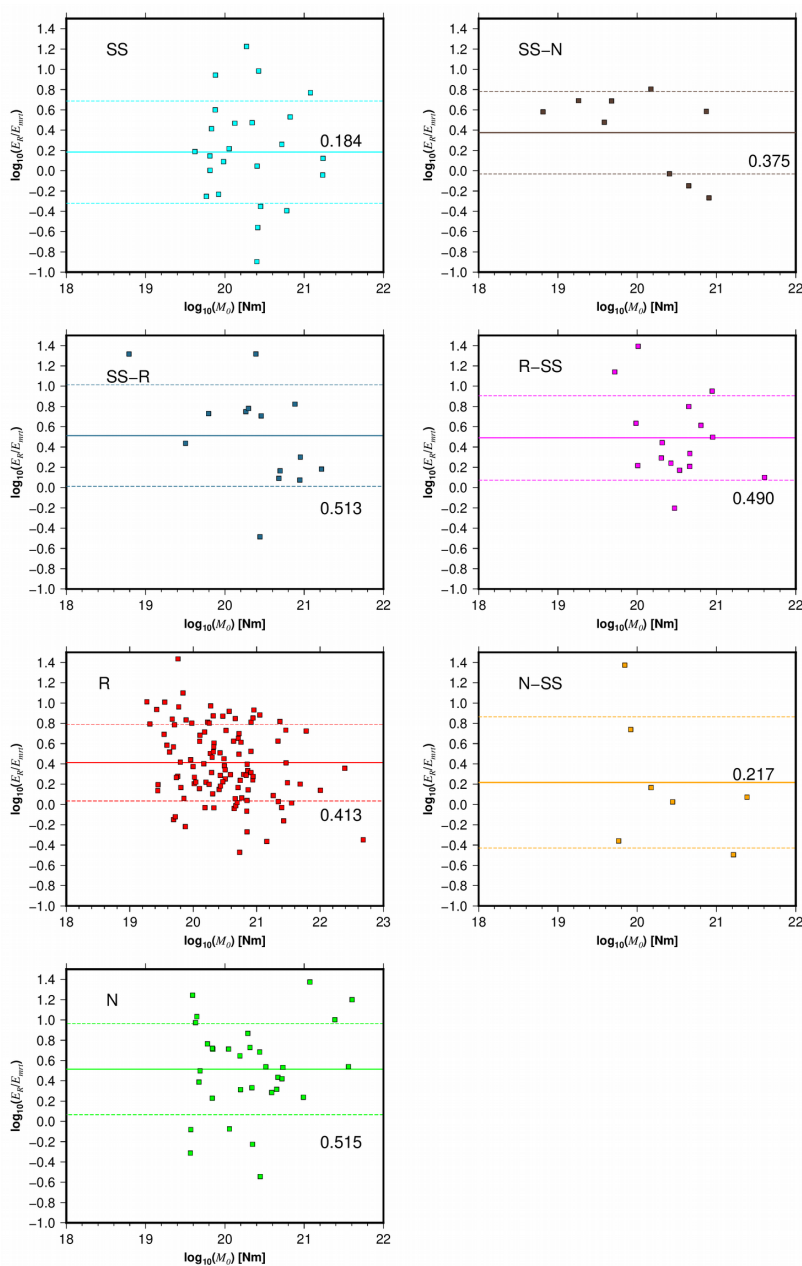
559

560 **Figure 7.** Comparison between radiated seismic energy based on velocity flux integration (E_R) and
561 overdamped (E_0) energy estimations. Lines represent the mean values (continuous) of different rupture
562 types and their standard deviation (dashed).



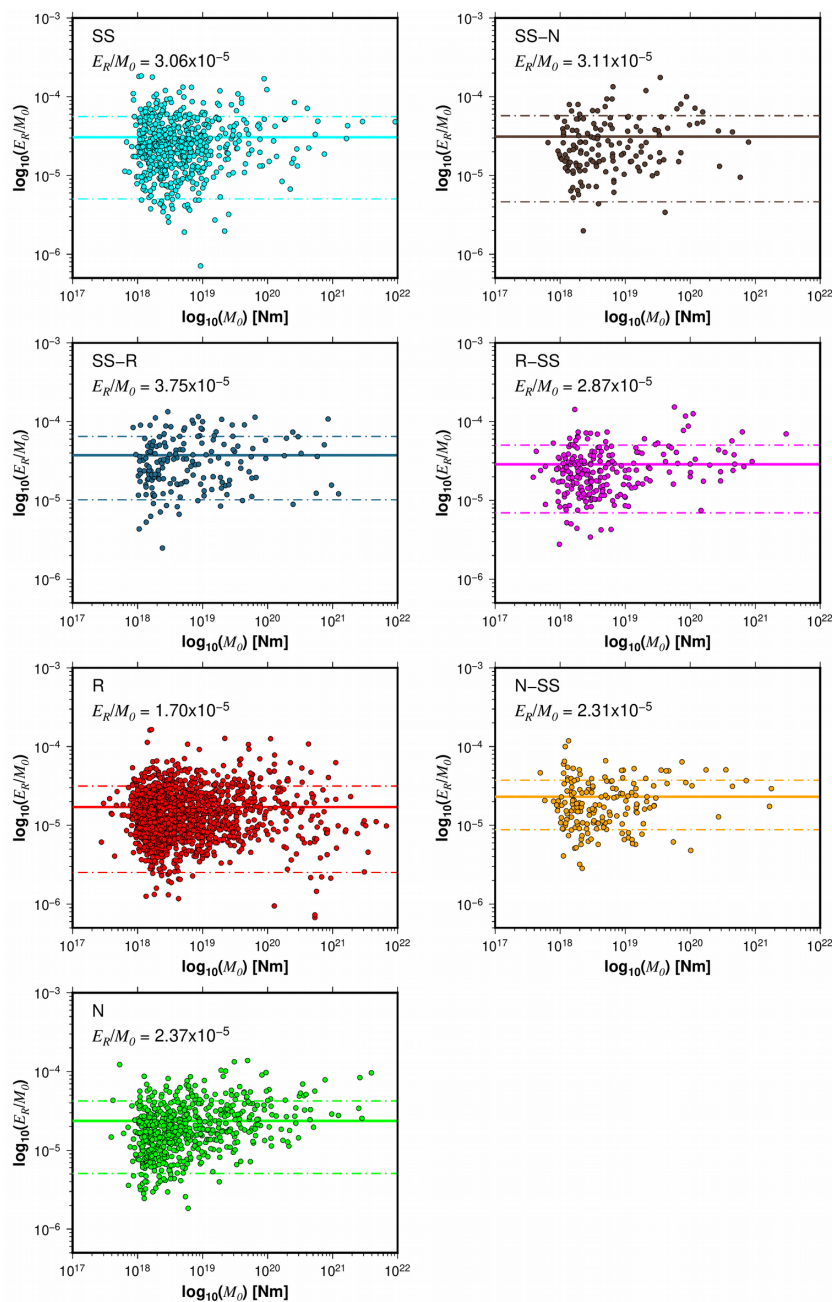
563

564 **Figure 8.** Comparison between the ratio of radiated seismic energy based on velocity flux integration
 565 (E_R) and averaged finite-fault model energy (E_U) estimations as a function of seismic moment. Lines
 566 represent the mean values (continuous) of different rupture types and their standard deviation (dashed).



567

568 **Figure 9.** Comparison between the ratio of radiated seismic energy based on velocity flux integration
 569 (E_R) and moment rate (E_{mr}) energy estimations as a function of seismic moment. Lines represent the
 570 mean values (continuous) of different rupture types and their standard deviation (dashed).

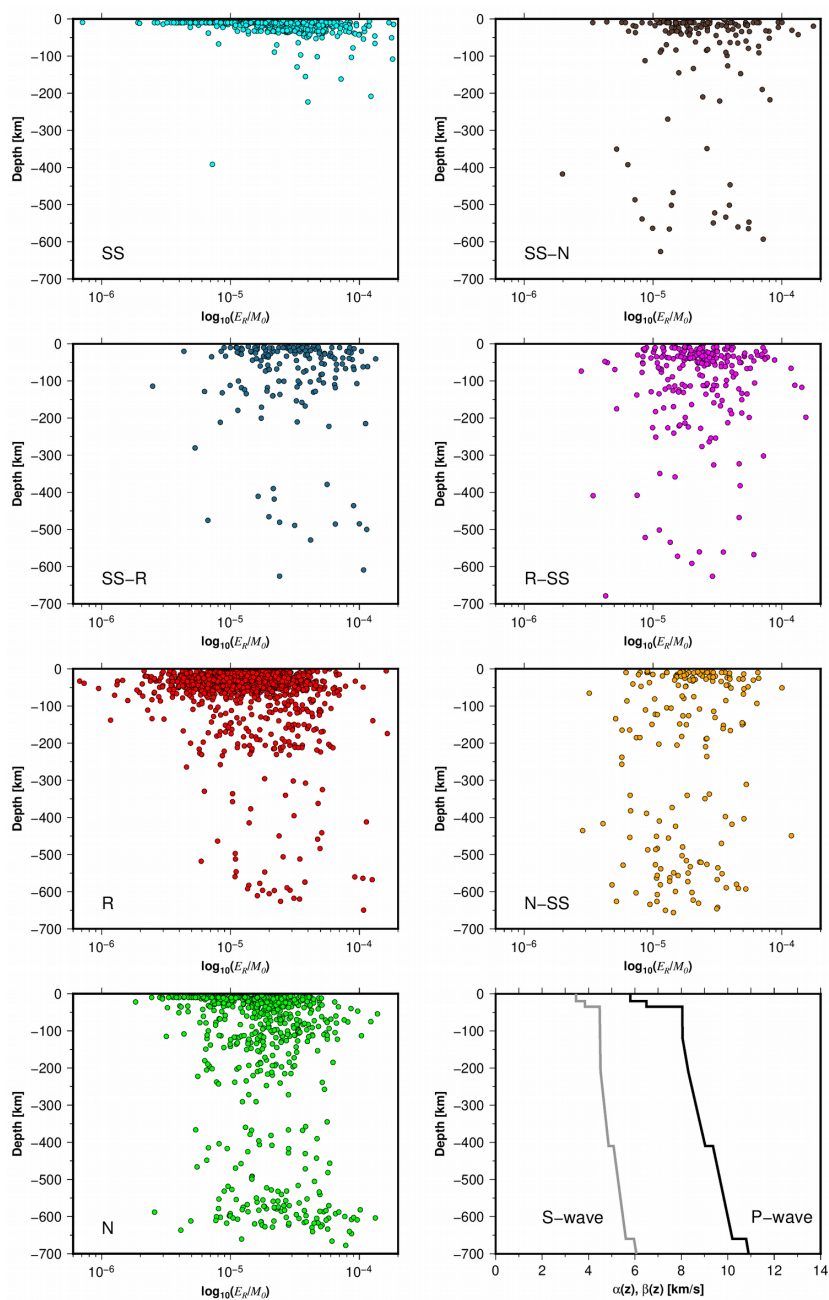


571

572 **Figure 10.** The estimated energy-to-moment ratios plotted as a function of the seismic moment for all

573 the rupture types. The solid and dashed lines show the mean value and standard deviations,

574 respectively.

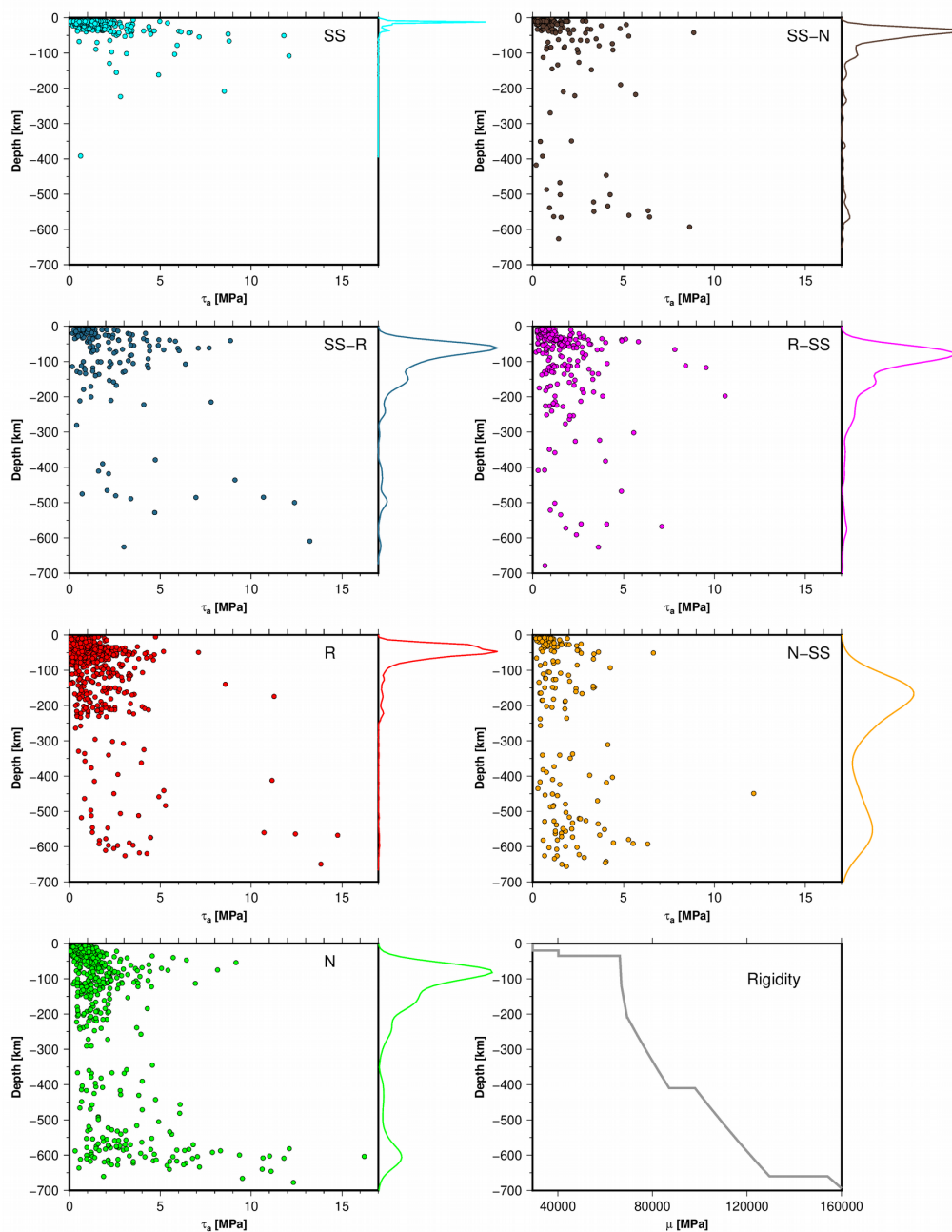


575

576 **Figure 11.** The calculated hypocentral depth for all the rupture types as a function of energy-to-moment

577 ratios. Lower right panel shows the ak135-F global velocity model.

578



579

580 **Figure 12.** Hypocentral depth for the different rupture subsets as a function of apparent stress (τ_a).

581 Color curves are the probability density functions (PDFs). Calculated rigidity as a function depth based

582 on the ak135-F global velocity model used to calculate τ_a (lower right panel).



583 **Table 1.** Regression results for the radiated seismic energy scaling relationships. The scaling relation is
 584 given by $\log_{10} E = a \log_{10} M_0 + b$, where E is the radiated seismic energy based on velocity flux
 585 integration (E_R), the overdamped dynamics approximation of the radiated energy (E_O), the energy
 586 obtained from the averaged finite-fault model (E_U), or the energy obtained from moment rate functions
 587 (E_{mrt}) in J, M_0 is the seismic moment in Nm. D^2 is the determination coefficient, a is the slope, Sa is the
 588 standard error of a , b is the intercept, and Sb is the standard error of b .

Parameter	a	Sa	b	Sb	D^2	Rupture type	Method
E_R [J]	1.04	0.02	-5.47	0.47	0.76	SS	Velocity flux integration
E_R [J]	1.09	0.04	-6.42	0.78	0.83	SS-N	Velocity flux integration
E_R [J]	1.05	0.03	-5.57	0.65	0.84	SS-R	Velocity flux integration
E_R [J]	1.10	0.03	-6.62	0.48	0.89	R-SS	Velocity flux integration
E_R [J]	1.01	0.01	-5.10	0.21	0.85	R	Velocity flux integration
E_R [J]	1.05	0.03	-5.72	0.64	0.84	N-SS	Velocity flux integration
E_R [J]	1.16	0.02	-7.67	0.33	0.87	N	Velocity flux integration
E_O [J]	1.14	0.16	-6.93	3.17	0.68	SS	Finite-fault model
E_O [J]	1.25	0.18	-9.35	3.67	0.87	SS-N	Finite-fault model
E_O [J]	0.88	0.17	-1.86	3.39	0.68	SS-R	Finite-fault model
E_O [J]	1.28	0.30	-10.21	6.18	0.51	R-SS	Finite-fault model
E_O [J]	0.86	0.07	-1.57	1.38	0.59	R	Finite-fault model
E_O [J]	1.27	0.13	-9.50	2.55	0.94	N-SS	Finite-fault model
E_O [J]	1.10	0.14	-6.26	2.80	0.65	N	Finite-fault model
E_U [J]	1.31	0.13	-11.85	2.56	0.81	SS	Finite-fault model
E_U [J]	1.51	0.19	-15.92	3.76	0.90	SS-N	Finite-fault model
E_U [J]	0.95	0.15	-4.86	3.06	0.75	SS-R	Finite-fault model
E_U [J]	1.40	0.20	-14.00	4.05	0.74	R-SS	Finite-fault model
E_U [J]	1.12	0.05	-8.44	1.03	0.81	R	Finite-fault model
E_U [J]	1.29	0.20	-11.68	4.11	0.87	N-SS	Finite-fault model
E_U [J]	1.09	0.09	-7.68	1.76	0.82	N	Finite-fault model
E_{mrt} [J]	1.23	0.15	-9.61	2.97	0.74	SS	Moment rate function
E_{mrt} [J]	1.32	0.21	-11.42	4.30	0.84	SS-N	Moment rate function
E_{mrt} [J]	1.08	0.07	-6.75	1.50	0.94	SS-R	Moment rate function
E_{mrt} [J]	1.44	0.18	-14.02	3.71	0.79	R-SS	Moment rate function
E_{mrt} [J]	1.02	0.07	-5.76	1.44	0.65	R	Moment rate function
E_{mrt} [J]	1.36	0.18	-12.25	3.61	0.91	N-SS	Moment rate function
E_{mrt} [J]	1.08	0.10	-6.68	2.05	0.77	N	Moment rate function

589
 590
 591
 592
 593
 594
 595
 596



597 **Table 2.** Conversion relationships among the different types of energies. E_R is the radiated seismic
 598 energy based on velocity flux integration, E_O is the overdamped dynamics approximation of the
 599 radiated energy, E_U is the energy obtained from the averaged finite-fault model, and E_{mrt} is the energy
 600 obtained from moment rate functions.

Rupture type	Parameters	Model	a	Sa	b	Sb	D^2
SS	E_R, E_O	$\log_{10}E_R = a \log_{10}E_O + b$	0.61	0.12	5.83	1.90	0.54
SS-N	E_R, E_O	$\log_{10}E_R = a \log_{10}E_O + b$	0.75	0.09	3.60	1.42	0.91
SS-R	E_R, E_O	$\log_{10}E_R = a \log_{10}E_O + b$	0.37	0.16	9.96	2.60	0.30
N-SS	E_R, E_O	$\log_{10}E_R = a \log_{10}E_O + b$	0.61	0.19	5.78	3.19	0.66
N	E_R, E_O	$\log_{10}E_R = a \log_{10}E_O + b$	0.59	0.10	6.23	1.67	0.52
R-SS	E_R, E_O	$\log_{10}E_R = a \log_{10}E_O + b$	0.44	0.12	8.90	1.95	0.49
R	E_R, E_O	$\log_{10}E_R = a \log_{10}E_O + b$	0.70	0.06	4.27	0.91	0.59
SS	E_R, E_U	$\log_{10}E_R = a \log_{10}E_U + b$	0.61	0.11	6.67	1.59	0.59
SS-N	E_R, E_U	$\log_{10}E_R = a \log_{10}E_U + b$	0.63	0.08	6.40	1.18	0.89
SS-R	E_R, E_U	$\log_{10}E_R = a \log_{10}E_U + b$	0.35	0.17	10.73	2.43	0.28
N-SS	E_R, E_U	$\log_{10}E_R = a \log_{10}E_U + b$	0.54	0.18	7.96	2.65	0.63
N	E_R, E_U	$\log_{10}E_R = a \log_{10}E_U + b$	0.78	0.11	4.50	1.62	0.61
R-SS	E_R, E_U	$\log_{10}E_R = a \log_{10}E_U + b$	0.56	0.11	7.82	1.58	0.66
R	E_R, E_U	$\log_{10}E_R = a \log_{10}E_U + b$	0.69	0.04	5.67	0.63	0.69
SS	E_R, E_{mrt}	$\log_{10}E_R = a \log_{10}E_{mrt} + b$	0.66	0.10	5.49	1.56	0.65
SS-N	E_R, E_{mrt}	$\log_{10}E_R = a \log_{10}E_{mrt} + b$	0.70	0.09	4.93	1.32	0.90
SS-R	E_R, E_{mrt}	$\log_{10}E_R = a \log_{10}E_{mrt} + b$	0.52	0.14	7.84	2.16	0.54
N-SS	E_R, E_{mrt}	$\log_{10}E_R = a \log_{10}E_{mrt} + b$	0.55	0.21	7.23	3.30	0.57
N	E_R, E_{mrt}	$\log_{10}E_R = a \log_{10}E_{mrt} + b$	0.78	0.11	3.81	1.79	0.60
R-SS	E_R, E_{mrt}	$\log_{10}E_R = a \log_{10}E_{mrt} + b$	0.62	0.10	6.41	1.50	0.75
R	E_R, E_{mrt}	$\log_{10}E_R = a \log_{10}E_{mrt} + b$	0.73	0.04	4.54	0.55	0.78

601
 602
 603
 604
 605
 606
 607
 608
 609
 610
 611
 612
 613
 614
 615
 616
 617
 618



619 **Table 3.** Estimations of average apparent stress (τ_α) for different faulting types based on the velocity
 620 flux integration method. τ_α is calculated with the following model: $\log_{10}E_R = \log_{10}M_0 + b$, where $\tau_\alpha = \mu$
 621 10^b . We assume $\mu = \bar{\mu}$ as the average rigidity in a specific depth interval of 30 km. τ_α^1 and τ_α^2 are the
 622 95% de upper and lower confidence intervals for the mean. 3 and 4 indicate τ_α results from Choy and
 623 Boatwright (1995) and Pérez-Campos and Beroza (2001), respectively (botton lines).

Depth [km]	$\bar{\mu}$ [MPa]	τ_α [MPa]							τ_α^1 [MPa]						τ_α^2 [MPa]							
		SS	SS-N	SS-R	N-SS	N	R-SS	R	SS	SS-N	SS-R	N-SS	N	R-SS	R	SS	SS-N	SS-R	N-SS	N	R-SS	R
0 ≤ z ≤ 30	3.48 × 10 ⁴	0.72	0.75	0.90	0.72	0.50	0.79	0.43	3.51	3.31	3.41	2.20	1.91	2.34	1.40	0.15	0.17	0.24	0.24	0.13	0.26	0.13
30 < z ≤ 60	5.33 × 10 ⁴	1.95	1.49	2.47	1.33	1.03	1.29	0.68	6.76	8.65	9.79	6.55	4.57	4.92	2.82	0.56	0.26	0.62	0.27	0.23	0.39	0.16
60 < z ≤ 90	6.65 × 10 ⁴	1.75		3.08	1.58		1.37	0.73	6.75		12.21	6.85		9.55	4.33	0.45		0.78	0.37		0.19	0.12
90 < z ≤ 120	6.67 × 10 ⁴	1.88			1.49		1.96	1.45	13.59			5.95		8.55	7.08	0.26		0.37		0.45	0.30	
120 < z ≤ 150	6.73 × 10 ⁴	1.22		1.15	1.13		1.38	0.90	5.55		6.57	3.76		5.43	7.86	0.27		0.20	0.34		0.35	0.10
150 < z ≤ 180	6.81 × 10 ⁴	1.55			1.38		3.93			7.79		0.61		0.24		0.29		0.33		0.30		
180 < z ≤ 210	6.90 × 10 ⁴	1.09			1.35		4.07			5.52		0.29		0.33		0.27		0.30		0.30		
210 < z ≤ 240	7.07 × 10 ⁴	1.19			1.34		5.17			6.04		0.27		0.30		0.27		0.30		0.30		
540 < z ≤ 570	1.16 × 10 ⁵	2.39			2.39		7.61			7.61		0.75		0.75		0.75		0.75		0.75		
570 < z ≤ 600	1.19 × 10 ⁵	2.88			2.88		14.88			14.88		0.56		0.56		0.56		0.56		0.56		
600 < z ≤ 630	1.23 × 10 ⁵	3.33			3.33		18.76			18.76		0.59		0.59		0.59		0.59		0.59		
	3.00 × 10 ⁵	3.55 ³		0.48 ³		0.32 ³		20.69 ³		4.16 ³		2.54 ³		0.61 ³		0.05 ³		0.04 ⁴		0.04 ⁴		
	3.00 × 10 ⁵	0.70 ⁴		0.25 ⁴		0.15 ⁴		1.01 ⁴		0.30 ⁴		0.19 ⁴		0.49 ⁴		0.21 ⁴		0.12 ⁴		0.12 ⁴		

624

625

626 **Table 4.** Estimations of average apparent stress (τ_α) for different faulting types based on slip
 627 distributions (E_{mt} , E_U , and E_O). τ_α is calculated with the following model: $\log_{10}E_R = \log_{10}M_0 + b$, where τ_α
 628 = $\mu 10^b$. We assume $\mu = \bar{\mu}$ as the average rigidity in a specific depth interval of 30 km. τ_α^1 and τ_α^2 are
 629 the 95% de upper and lower confidence intervals for the mean. 3 and 4 indicate τ_α results from Choy
 630 and Boatwright (1995) and Pérez-Campos and Beroza (2001), respectively (botton lines).

Depth [km]	$\bar{\mu}$ [MPa]	τ_α [MPa]							τ_α^1 [MPa]						τ_α^2 [MPa]								
		SS	SS-N	SS-R	N-SS	N	R-SS	R	SS	SS-N	SS-R	N-SS	N	R-SS	R	SS	SS-N	SS-R	N-SS	N	R-SS	R	
E_{mt}																							
0 ≤ z ≤ 30	3.48 × 10 ⁴	0.52		0.33		0.31		0.16		5.72		1.36		2.10		1.47		0.05		0.08		0.05	
30 < z ≤ 60	5.33 × 10 ⁴	0.33		0.31		0.24		5.72		1.36		2.10		1.47		2.28		0.05		0.08		0.03	
E_U																							
0 ≤ z ≤ 30	3.48 × 10 ⁴	2.78		1.41		2.59		1.50		32.77		23.19		21.79		19.92		0.24		0.08		0.11	
30 < z ≤ 60	5.33 × 10 ⁴	2.78		1.41		2.59		1.50		32.77		23.19		21.79		19.92		0.24		0.08		0.17	
E_O																							
0 ≤ z ≤ 30	3.48 × 10 ⁴	0.10		0.04		0.04		0.03		0.91		0.51		0.24		0.17		0.01		0.01		0.005	
30 < z ≤ 60	5.33 × 10 ⁴	0.10		0.04		0.04		0.03		0.91		0.51		0.24		0.25		0.01		0.01		0.007	
	3.00 × 10 ⁵	3.55 ³		0.48 ³		0.32 ³		20.69 ³		4.16 ³		2.54 ³		0.61 ³		0.05 ³		0.04 ⁴		0.04 ⁴		0.04 ⁴	
	3.00 × 10 ⁵	0.70 ⁴		0.25 ⁴		0.15 ⁴		1.01 ⁴		0.30 ⁴		0.19 ⁴		0.49 ⁴		0.21 ⁴		0.12 ⁴		0.12 ⁴		0.12 ⁴	

631